The object of this study is the delay and direction of arrival (DOA) of wideband signals in additive noise observed by a synchronized two-channel receiving system. The problem is that most wideband delay and DOA estimation methods rely on multi-stage or iterative procedures – such as peak search, covariance and eigen-decomposition, angular scanning, or sparse recovery – which increase computational load and restrict real-time applicability.

The essence of the obtained results is a unified spectral-correlation model that enables joint estimation of delay and DOA directly from the phase of the complex cross-spectrum. The delay is determined from the linear phase slope with respect to frequency, while the DOA is obtained from a deterministic phase offset defined by the known antenna baseline. This formulation eliminates iterative refinement and angular scanning and reduces computational complexity to $O(N\log_2 N)$.

Numerical experiments with linear frequency-modulated signals in Gaussian noise demonstrate predictable accuracy behavior: with increasing signal-to-noise ratio, the DOA root-mean-square error decreases from 0.15–0.18° to 0.03–0.04°, while the delay error decreases from tens of nanoseconds to a few nanoseconds.

These results are explained by the deterministic relationship between time shifts, spatial delays, and phase behavior in the frequency domain under stationary noise conditions. The proposed model can be applied in practice for synchronized two-channel wideband reception with known geometry and fixed antenna baseline in real-time passive monitoring and direction-finding systems

Keywords: spectral-correlation analysis, mathematical modeling, one-pass estimation, time delay and direction of arrival, wideband signals

UDC 519.688:621.396.67
DOI: 10.15587/1729-4061.2026.352271

DEVELOPMENT OF A UNIFIED SPECTRAL-CORRELATION PHASE MATHEMATICAL MODEL FOR SINGLE-PASS JOINT ESTIMATION OF TIME DELAY AND DIRECTION OF ARRIVAL IN NOISY WIDEBAND SIGNALS

Anar Khabay
PhD, Associate Professor
Department of Electronics, Telecommunications and Space Technologies*
Department of Automation and Robotics
Almaty Technological University
Tole bi str., 100, Almaty, Republic of Kazakhstan, 050012
ORCID: https://orcid.org/0000-0002-0409-1531

Nurzhigit Smailov
PhD, Professor**
Department of Radio Engineering, Electronics and Space Technologies*
ORCID: https://orcid.org/0000-0002-7264-2390

Gulbakhar Yussupova
PhD
Department of Radio Engineering and Telecommunications
ALT University
Shevchenko str., 97, Almaty, Republic of Kazakhstan, 050010
ORCID: https://orcid.org/0000-0001-9765-2221

Amandyk Tuleshov
Doctor of Technical Sciences, Professor**
ORCID: https://orcid.org/0000-0001-9775-3049

Valentyn Tsyporenko
PhD***
ORCID: https://orcid.org/0000-0002-6843-8960

Vitaliy Tsyporenko
PhD***
ORCID: https://orcid.org/0000-0001-8559-006X

Zhandos Dosbayev
PhD**
Department of Radio Engineering, Electronics and Space Technologies*
ORCID: https://orcid.org/0000-0003-1673-4036

Gulden Khairusheva
Master, Senior Lecturer
Department of Technical Disciplines
Kazakhstan University Innovation and Telecommunications Systems
Mametova str., 81, Uralsk, Republic of Kazakhstan, 090006
ORCID: https://orcid.org/0009-0006-0652-5088

Akezhan Sabibolda
Corresponding author
PhD**
Department of Cyber Security and Information Technology
Almaty Academy of Ministry of Internal Affairs
Utepov str., 29, Almaty, Republic of Kazakhstan, 050060
E-mail: sabibolda98@gmail.com
ORCID: https://orcid.org/0000-0002-1186-7940

*Satbayev University
Satbayev str., 22, Almaty, Republic of Kazakhstan, 050013
**Institute of Mechanics and Mechanical Engineering named after Academician U. A. Dzholdasbekov
Kurmangazy str., 29, Almaty, Republic of Kazakhstan, 050010
***Department of Biomedical Engineering and Telecommunications
Zhytomyr Polytechnic State University
Chudnivska str., 103, Zhytomyr, Ukraine, 10005

Received 03.12.2025
Received in revised form 28.01.2026
Accepted 12.02.2026
Published 27.02.2026

How to Cite: *Khabay, A., Smailov, N., Yussupova, G., Tuleshov, A., Tsyporenko, V., Tsyporenko, V., Dosbayev, Z., Khairusheva, G., Sabibolda, A. (2026). Development of a unified spectral-correlation phase mathematical model for single-pass joint estimation of time delay and direction of arrival in noisy wideband signals. Eastern-European Journal of Enterprise Technologies, 1 (4 (139)), 19–35. https://doi.org/10.15587/1729-4061.2026.352271*

1. Introduction

The task of determining time delays and directions of arrival (DOA) for wideband signals remains a foundational problem in applied mathematics, with direct relevance to passive sensing, monitoring, and localization technologies. It plays a central role in systems such as radio-monitoring platforms, passive direction-finding arrays, spectrum surveillance

setups, and distributed receivers that operate without emitting their own signals. In these systems, parameter estimation is carried out using spatially distributed receivers with known geometry, while observed signals are typically affected by additive noise, limited sampling rates, and finite bandwidth constraints [1, 2].

Accurate and computationally efficient estimation of delay and DOA is crucial in real-world applications. Algorithms must function with limited processing resources, operate in real-time, and maintain low latency – particularly in mobile and autonomous platforms [3]. These constraints often restrict the use of complex synchronization schemes or hardware-intensive receiver architectures, limiting reliance on computationally heavy or iterative algorithms.

Traditional correlation-based approaches remain widely used for time-delay estimation in such contexts. These methods, which involve computing cross-correlation functions and detecting peaks, typically have quadratic complexity $O(N^2)$, where N is the observation window length [4, 5]. For wideband signals or longer integration times, this becomes a limiting factor for real-time performance. Frequency-domain implementations using Fast Fourier Transforms can reduce complexity to $O(N\log_2 N)$, but still require multiple processing steps, including spectral estimation, inverse transforms, peak detection, and subsequent spatial processing.

A key drawback of many existing solutions is that delay and DOA are estimated together via sequential stages – often involving covariance computations, eigenvalue decompositions, scanning procedures, or grid-based optimizations. While effective, such pipelines increase computational load and latency, making them less suitable for systems requiring fast and deterministic performance [6].

At the same time, many modern receivers already compute spectral representations as part of signal analysis pipelines. In wideband systems, time delay appears as a frequency-dependent phase shift, and spatial separation introduces an additional deterministic phase difference due to antenna geometry. Yet, methods that exploit this spectral phase structure for direct joint estimation of temporal and spatial parameters are rarely applied.

Therefore, studies that are devoted to research focused on the efficient joint estimation of propagation time delay and direction of arrival for noisy wideband signals remain of high scientific relevance in contemporary signal-processing studies. The rapid advancement of passive monitoring systems, spectrum surveillance platforms, autonomous sensing networks, and real-time localization technologies demands parameter-estimation methods that are computationally efficient, predictable in performance, and robust under bandwidth constraints and significant noise contamination.

The practical significance of this line of research lies in its potential to improve passive direction-finding and localization architectures while enabling real-time implementation with reduced computational overhead. Methods that maintain clear physical interpretability of estimated parameters enhance system transparency and facilitate integration into operational platforms. Furthermore, unified spectral-correlation frameworks provide a basis for compact and energy-efficient receiver designs, thereby increasing the precision, scalability, and functional capabilities of modern monitoring and sensing systems operating in wideband environments.

2. Literature review and problem statement

The work reported in [1] presents a wideband DOA estimation approach that combines correlation-domain processing with array-manifold interpolation. The authors show that this method improves angular resolution and estimation accuracy, particularly at low signal-to-noise ratios, by compensating for mismatches between wideband steering vectors and narrowband array models. However, unresolved issues remain related to the multi-stage nature of the processing chain and the need for careful tuning of interpolation and correlation parameters across different bandwidths and array configurations. The reason for these limitations lies in the separation between correlation-domain processing and spatial parameter recovery, which increases algorithmic complexity. As a result, the approach becomes less suitable for joint delay and DOA estimation under strict real-time constraints.

In work [2], a wideband DOA estimation method is proposed for scenarios where the number of sources is unknown. It is shown that reliable DOA estimates can be obtained by exploiting frequency-domain subspace orthogonality and weighted covariance formulations without prior source enumeration. Nevertheless, unresolved issues are associated with the need for repeated covariance estimation and subspace decomposition across multiple frequency bins. The reason for this is the reliance on subspace-based processing, which inherently increases computational cost. Moreover, the method focuses exclusively on DOA recovery, so additional processing stages are required for time-delay estimation, making joint estimation computationally inefficient for real-time applications.

The study in paper [3] investigates wideband DOA estimation using compressive-sensing techniques applied to generalized coprime arrays. The authors show that reduced measurement dimensionality can lower computational load without sacrificing angular resolution. However, unresolved issues arise due to the dependence on sparsity assumptions, grid discretization, and regularization parameter selection. These limitations stem from the optimization-based nature of compressive-sensing methods, which affects reproducibility and robustness. In addition, time-delay estimation is not incorporated into the framework, limiting its applicability for joint delay and DOA recovery in practical monitoring systems.

A fractional Fourier transform-based approach to wideband DOA estimation is introduced in work [4]. It is shown that by exploiting the energy concentration properties of linearly frequency-modulated signals, inter-element delays can be estimated and used to infer DOA. Nevertheless, unresolved issues remain because the method is inherently multi-stage and strongly dependent on assumed signal structures. The reason for this limitation is the reliance on specific modulation characteristics, which restricts extension to general broadband signals encountered in real monitoring environments. Consequently, the approach is not suitable as a unified framework for joint delay and DOA estimation.

In work [5], the computational efficiency of wideband DOA estimation is improved through interpolation-based acceleration techniques. The authors demonstrate that these methods reduce the numerical burden of estimator evaluation. However, unresolved issues persist since the underlying multi-frequency processing and parameter-search architecture remains unchanged. The reason for this is that interpolation accelerates evaluation but does not alter the fundamental estimation structure. Furthermore, propagation delay is not incorporated as a jointly estimated parameter, which limits the applicability of the method for unified delay – DOA estimation.

Robust time-delay estimation for wideband signals in non-Gaussian noise environments is examined in paper [6]. It is shown that heavy-tailed noise distributions can cause

outliers in classical correlation-based estimators, and more robust alternatives are proposed. Despite improved reliability, unresolved issues remain because the analysis is limited to delay estimation between sensor pairs and does not address direction-of-arrival estimation. The reason for this limitation lies in the focus on robustness mechanisms, which introduce additional processing complexity. As a result, deterministic real-time implementation of joint delay and DOA estimation remains impractical.

The concept of wideband direction finding using phase correlation in time-modulated antenna arrays is explored in paper [7]. The authors show that leveraging phase relationships across frequency components improves robustness compared to magnitude-based approaches. However, unresolved issues are related to the reliance on specialized antenna architectures and modulation schemes. The reason for this limitation is that phase correlation is tightly coupled with array design. In addition, the method focuses exclusively on DOA estimation, while propagation delay must be handled separately, preventing unified joint estimation.

In work [8], an initialization-free coherent subspace-based wideband DOA estimation technique is proposed. It is shown that removing coarse initial estimates improves angular stability through focused covariance processing. Nevertheless, unresolved issues remain due to the continued reliance on eigenvalue decomposition and multi-frequency covariance analysis. The reason for this is the inherent complexity of subspace-based methods. Moreover, time-delay estimation is not incorporated within the model, which limits its suitability for joint parameter recovery in real-time systems.

Spectral-correlation-based delay estimation is investigated in paper [9]. The authors show that analysis of the complex cross-spectrum can reveal temporal and spatial information with enhanced noise robustness compared to time-domain correlation. However, unresolved issues persist because the estimation procedure remains multi-stage and lacks a unified analytical formulation that directly links spectral phase to joint delay and DOA recovery. The reason for this limitation lies in the absence of a single-pass analytical model. In addition, computational complexity is not explicitly characterized, complicating real-time applicability.

In work [10], machine-learning techniques are introduced to enhance spectral-correlation-based delay and DOA estimation under interference and noise. It is shown that data-driven models can improve estimation accuracy. Nevertheless, unresolved issues arise due to dependence on training data, additional computational steps, and model generalization limits. The reason for this is the non-deterministic nature of learning-based approaches. Consequently, the multi-stage structure of the estimation pipeline is preserved, limiting deterministic real-time deployment.

However, despite extensive progress in wideband delay and direction-of-arrival estimation, existing methods predominantly rely on multi-stage or iterative processing schemes, such as covariance-based subspace decomposition, frequency focusing, angular scanning, or learning-assisted refinement. These approaches increase algorithmic complexity and obscure the direct physical relationship between cross-spectral phase behavior and propagation parameters. In particular, the phase structure of the complex cross-spectrum has not been fully exploited as a deterministic basis for unified, single-pass estimation of both time delay and direction of arrival. As a result, the accuracy, robustness to noise, and computational characteristics of one-pass spectral-correlation estimation frameworks remain insufficiently investigated and quantitatively justified.

3. The aim and objectives of the study

The aim of this study is to develop a unified spectral-correlation mathematical model for single-pass joint estimation of propagation time delay and direction of arrival of noisy wideband signals based on the phase structure of the complex cross-spectrum. The developed model enables deterministic estimation with reduced computational complexity and physically interpretable recovery of temporal and spatial parameters, thereby supporting reliable real-time application in passive wideband direction-finding systems.

To achieve this aim, the following objectives are accomplished:

– to establish the structural framework of the unified spectral-correlation model that provides a deterministic single-pass transformation of cross-spectral phase information into propagation delay and direction-of-arrival parameters;

– to investigate the estimation accuracy of the proposed model under practical conditions, including variations of signal-to-noise ratio, antenna baseline, and spectral windowing, with quantitative evaluation of delay and angular errors;

– to perform a comparative analysis of the proposed one-pass spectral-correlation model with existing wideband delay and direction-finding methods, focusing on estimation accuracy, computational structure, and algorithmic complexity.

4. Materials and Methods

The object of this study is the time delay and direction of arrival of wideband signals in additive noise observed by a synchronized two-channel receiving system. The study is carried out through analytical formulation of a spectral-correlation mathematical model and its numerical validation under controlled simulation conditions. Frequency-domain signal representations and the phase structure of the complex cross-spectrum are employed, without considering the development of specialized hardware architectures or novel antenna configurations [11].

The central hypothesis of the study is that temporal and spatial propagation parameters are deterministically encoded within the phase of the complex cross-spectrum between spatially separated receiving channels. Unlike classical correlation-based and subspace-based approaches that rely on multi-stage processing, peak searching, covariance decomposition, or iterative optimization, the proposed method enables direct analytical recovery of both time delay and direction of arrival within a single computational pass [12]. This formulation ensures mathematical transparency and predictable computational complexity dominated by fast Fourier transform operations.

The received signals are modeled as wideband stochastic processes contaminated by additive white Gaussian noise with stationary statistical properties, consistent with commonly adopted spectral and correlation-based signal models [13, 14]. The receiving system geometry is assumed to be known and fixed, providing a deterministic relationship between spatial separation and phase offset in the frequency domain. Sufficient signal bandwidth is assumed to ensure reliable estimation of phase slopes across frequency components, and signal sampling follows the Nyquist criterion.

Spectral representations are obtained using discrete Fourier transform-based processing.

To clearly define the methodological scope, several explicit assumptions and controlled simplifications are adopted. The receiving system is limited to a two-channel configuration in order to establish a direct analytical relationship between propagation delay, spatial displacement, and spectral phase behavior. Noise processes are assumed to be additive, white, Gaussian, and statistically independent across channels. Propagation is considered to occur under free-space conditions without multipath effects, shadowing, or non-stationary interference. Perfect synchronization between receiving channels and exact knowledge of antenna baseline geometry are assumed. No adaptive filtering, learning-based compensation, or iterative refinement mechanisms are incorporated, ensuring that all estimation results arise solely from deterministic spectral-correlation processing.

For numerical validation, the transmitted wideband signal is generated as a linear frequency-modulated waveform with prescribed bandwidth, center frequency, and pulse duration. Propagation delay is introduced analytically according to the known receiver geometry and assumed direction of arrival. Additive noise levels are systematically varied to span a broad range of signal-to-noise ratios, enabling evaluation of estimation performance under noise-dominated, transitional, and high-quality observation conditions. Discretization length, sampling frequency, antenna baseline, and spectral windowing functions are selected to provide adequate spectral resolution and stable phase estimation.

Analytical modeling is performed using Mathcad 11.0b (PTC Inc., USA), which enables symbolic formulation, parametric analysis, and visualization of analytical expressions. Numerical signal generation, spectral processing, Monte-Carlo simulations, and performance evaluation are implemented in Python 3.11 (Python Software Foundation, USA) using the PyCharm 2022.2.4 Community Edition integrated development environment (JetBrains, Czech Republic). This analytical-numerical workflow ensures transparent parameter control and reproducible simulation results. All numerical simulations were executed on an ASUS TUF Gaming 17 laptop equipped with an Intel Core i7-13620H CPU, 16 GB RAM, and an NVIDIA GeForce RTX 4050 GPU.

The methodological foundation follows established spectral and correlation-based approaches for time-delay and direction-of-arrival estimation widely used in signal processing research [15–18]. Classical generalized cross-correlation and FFT-based frequency-domain implementations serve as computational baselines, where time-domain correlation exhibits quadratic computational complexity with respect to observation length, while covariance-based and subspace-based wideband DOA estimators involve eigen-decomposition with cubic complexity in the number of receiving channels [19–21]. These characteristics motivate the adoption of spectral-correlation processing as a computationally efficient alternative.

The spectral-correlation approach exploits frequency-domain phase behavior that is inherently insensitive to amplitude distortions and benefits from noise averaging across frequency bins [22, 23]. Overall computational complexity is reduced to quasi-linear order dominated by FFT operations, enabling real-time applicability. Analytical predictions are systematically validated through numerical experiments across varying signal-to-noise ratios, windowing strategies, and antenna baseline lengths, ensuring both theoretical soundness and practical relevance.

5. Results of the spectral-correlation single-pass time delay and direction-of-arrival estimation

5. 1. Structural framework of the unified spectral-correlation mathematical model

5. 1. 1. Geometric configuration and reference propagation delay

The development of the spectral-correlation model begins with a formal definition of the physical and geometrical framework of the signal propagation problem. The goal is to establish an exact analytical link between the DOA of a wideband signal and the spatial configuration of the receiver system, as well as the resulting propagation delay [24]. This relation forms the basis for evaluating estimation accuracy.

The receiver is modeled as a two-element spatial array with a known fixed antenna baseline, denoted b_a, which represents the distance between the receiving elements. Signal propagation is assumed to occur in free space at a constant speed c, corresponding to the speed of light. These ideal conditions allow the propagation time delay τ between the channels to be determined purely by system geometry and the direction of arrival θ of the incoming signal, eliminating uncertainty from medium effects [25].

The geometric configuration of the two-element receiving system, together with the definition of the direction-of-arrival angle θ and the corresponding propagation delay τ, is illustrated in Fig. 1. The incoming signal's direction is constrained between 0–180°, covering all physical approach angles relative to the receiver baseline. For analytical consistency with trigonometric and spectral-domain analysis, the angle is expressed in radians.

1. Setting the initial conditions

Set the angle of arrival of the radio signal in the range from 0 to 180°:

$$\theta_{grad} := 50$$

Convert degrees to radians:

$$\theta_{rad} := \frac{(\theta_{grad} \cdot \pi)}{180} \qquad \theta_{rad} = 0.8727$$

Set the antenna baseline, m:

$$b_a := 2500$$

Set the speed of light constant, m/s:

$$c := 299792458$$

Compute the propagation delay corresponding to the given initial conditions, s:

$$\tau := \frac{b_a \cdot \cos(\theta_{rad})}{c} \qquad \tau = 5.3603 \times 10^{-6}$$

Fig. 1. Geometry of the two-element receiving system and definition of the direction-of-arrival angle and propagation delay

Using basic geometric relations, the propagation delay τ is explicitly defined as a function of the antenna baseline b_a, the arrival angle θ, and the propagation velocity c, forming the reference value against which estimates are compared [26].

Fig. 1 depicts the spatial layout – baseline, wavefront, and associated delay – forming the physical foundation of the model. This structure ensures consistent reference geometry across all steps of signal generation, spectral processing, and correlation-based analysis.

5. 1. 2. Analytical modeling of the wideband linear frequency-modulated signal

After establishing the propagation geometry and reference delay, the transmitted wideband signal is analytically modeled as a linear frequency-modulated (LFM) waveform. The signal amplitude S_0 defines the peak magnitude of the transmitted waveform, while the initial phase Φ_0 determines the starting phase offset and is set to zero to eliminate phase ambiguity at the signal origin [27, 28]. The signal duration T_s specifies the observation interval for subsequent spectral analysis.

The frequency modulation is characterized by the signal bandwidth b and the center frequency f_0, which together control the instantaneous frequency sweep across the wideband spectrum. The resulting phase law contains a linear term associated with the carrier frequency and a quadratic term corresponding to linear frequency modulation, producing the characteristic chirp structure.

The analytical expressions defining the original signal $S_1(t)$ and the delayed signal $S_2(t)$, obtained by introducing the propagation delay τ into the time argument, are illustrated in Fig. 2. This formulation ensures that the time delay manifests as a deterministic phase shift in the frequency domain, enabling subsequent spectral-correlation-based estimation.

2. Signal generation

2.1 Generation of the first signal

Set the signal amplitude, V:

$S_0 := 100$

Set the initial phase of the signal in degrees and convert it to radians:

$\Phi_{grad} := 0 \qquad \Phi o := \frac{(\Phi_{grad} \cdot \pi)}{180} \qquad \Phi o = 0$

Set the signal period, s:

$T_s := \left(1000 \times 10^{-6}\right) \qquad T_s = 1 \times 10^{-3}$

Set the signal bandwidth, Hz:

$b := 0.38 \times 10^{9}$

Set the center frequency of the signal, Hz:

$f_0 := 500 \cdot 10^{6}$

Define the first signal:

$S1(t) := S_0 \cdot \sin\left[\Phi o + 2 \cdot \pi \cdot \left(f_0 \cdot t + b \cdot t^2\right)\right]$

Define the second signal by introducing the previously known delay τ into the signal expression:

$S2(t) := S_0 \cdot \sin\left[\Phi o + 2 \cdot \pi \cdot \left[f_0 \cdot (t - \tau) + b \cdot (t - \tau)^2\right]\right]$

Fig. 2. Analytical generation of the wideband linear frequency-modulated (LFM) signal

The time-frequency-phase relationship is preserved in the analytical LFM signal, ensuring the geometry-induced delay remains encoded in the signal throughout spectral transformation and correlation procedures.

To visually confirm the correctness of the signal model, time-domain plots of the original and delayed signals are compared, as shown in Fig. 3, 4. The first represents the reference wideband signal, while the second includes the geometry-induced propagation delay [29]. These graphs validate correct time-domain delay modeling prior to discretization and subsequent spectral processing.

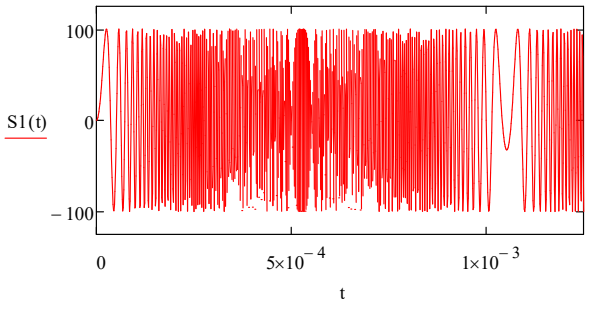

Fig. 3. Time-domain representation of the first wideband signal $S_1(t)$ generated using a linear frequency-modulated waveform

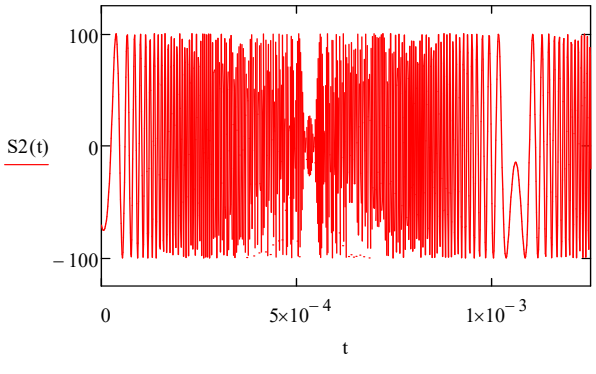

Fig. 4. Time-domain representation of the delayed wideband signal $S_2(t)$

The analytical and delayed signals serve as inputs to further steps: discretization, windowing, noise simulation, spectral transformation, and the core spectral-correlation-based estimation of delay and DOA.

5. 1. 3. Discretization and windowing strategy

For analytical spectral processing, the wideband signal is sampled into discrete time. Sampling is performed at a fixed rate F_d, yielding a finite sequence of N uniformly spaced samples suitable for discrete Fourier transform (DFT) analysis [30]. The corresponding sampling interval is defined as $T_d = 1 / F_d$, and the discrete time grid is given by $t_k = kT_d$, where k denotes the sample index ranging from 0 to $N - 1$. The total analysis time $t\text{Max} = NT_d$ is selected to fully cover the duration of the wideband signal pulse, ensuring complete energy capture within a single processing frame.

The definition of the discretization parameters, sampling grid, and analysis time interval used for window-based signal processing is illustrated in Fig. 5.

Before frequency-domain transformation, the discrete signal sequence is multiplied by a window function $W_i(k)$

applied pointwise to each sample index k in order to control spectral leakage and improve phase stability across frequency bins. Several classical window functions are considered in this study, including the rectangular window $W_1(k)$, Blackman window $W_2(k)$, Hann window $W_3(k)$, Kaiser window $W_4(k)$, and Hamming window $W_5(k)$, each characterized by different main-lobe widths and side-lobe attenuation properties [31].

The mathematical definitions of these window functions as functions of the discrete sample index k and total sample number N are presented in Fig. 6. The use of multiple window types within the same processing framework allows systematic assessment of their influence on spectral-correlation estimation accuracy.

3. Window generation

3.1. Definition of window discretization parameters

Set the number of samples:

$N := 65536$

Set the sampling frequency, Hz:

$Fd := 32.8 \cdot 10^6$

Set the sampling period, s:

$Td := \frac{1}{Fd} \qquad Td = 3.0488 \times 10^{-8}$

Define the analysis time equal to the duration of the wideband signal pulse, s:

$tMax := N \cdot Td \qquad tMax = 1.998 \times 10^{-3}$

Define the discrete time index:

$k := 0 .. N - 1 \qquad t_k := k \cdot Td$

Fig. 5. Definition of discretization parameters and time grid for window-based signal analysis

3.2. Window functions

3.2.1. Rectangular window:

$$W_1(k) := \begin{cases} 1 & \text{if } k \le N \\ 0 & \text{otherwise} \end{cases}$$

3.2.2. Blackman window:

$$W_2(k) := 0.42 + \frac{1}{2} \cdot \cos\left[\frac{2 \cdot \pi \cdot \left(k - \frac{N}{2}\right)}{N}\right] + 0.08 \cdot \cos\left[\frac{4 \cdot \pi \cdot \left(k - \frac{N}{2}\right)}{N}\right]$$

3.2.3. Hann window:

$$W_3(k) := 0.5 \cdot \left(1 - \cos\left(\frac{2 \cdot \pi k}{N}\right)\right)$$

3.2.4. Kaiser window:

$$W_4(k) := \frac{I0\left[4 \cdot \sqrt{1 - \left[\frac{(2 \cdot k - N + 1)}{N}\right]^2}\right]}{I0(4)}$$

3.2.5.Hamming window:

$$W_5(k) := 0.53836 - 0.46164 \cdot \cos\left(\frac{2 \cdot \pi k}{N}\right)$$

Fig. 6. Mathematical definitions of window functions used for spectral analysis

These windowed discrete signals form the input for subsequent frequency-domain operations: Fourier transform, cross-spectrum construction, and phase extraction – all central to the spectral-correlation estimation process.

5. 1. 4. Noise modeling and signal-to-noise ratio control

To replicate realistic observational conditions, additive noise is introduced into the discrete-time signals. The noise in each receiving channel is modeled as a statistically independent Gaussian random sequence characterized by zero mean values μ_1 and μ_2 and standard deviations σ_1 and σ_2, respectively. These parameters define the variance of the noise processes and ensure controlled statistical behavior consistent with classical additive white Gaussian noise assumptions widely used in spectral and correlation-based signal processing.

The generated noise sequences $Noise_1$ and $Noise_2$ are produced as random realizations of length N and scaled by the corresponding standard deviations, while the factor J is used as a normalization coefficient in the numerical implementation. The signal-to-noise ratio (SNR) is estimated using the ratio between the signal amplitude S_0 and the noise standard deviation, expressed in logarithmic scale.

Using a Gaussian noise model allows controlled analysis of noise impact on spectral-correlation phase behavior. The noise variance is adjusted to maintain prescribed SNR levels throughout numerical experiments, enabling systematic evaluation of estimation performance under different noise conditions. Each receiving channel is assigned an independent noise realization to avoid artificial correlation effects.

The procedure for generating Gaussian noise in both receiving channels and estimating the corresponding signal-to-noise ratio is illustrated in Fig. 7. Sample excerpts of the generated noise confirm zero-mean behavior and statistical independence across channels, while time-domain plots further illustrate the stochastic nature of the interference.

4. Noise generation with normal distribution

Set the standard deviation:

$\sigma_1 := 71 \qquad \sigma_2 := \sigma_1 \qquad J := 1$

Set the mean value:

$\mu_1 := 0 \qquad \mu_2 := 0$

Signal-to-noise ratio estimate:

$20 \cdot \log\left(\frac{S_0}{\sqrt{2} \cdot \sigma_1}\right) = -0.0355$

Generate Gaussian noise in the first and second channels:

$Noise1 := J \cdot rnorm(N, \mu_1, \sigma_1) \qquad Noise2 := J \cdot rnorm(N, \mu_2, \sigma_2)$

Fig. 7. Generation of Gaussian noise with normal distribution in two reception channels and estimation of the signal-to-noise ratio

Sample excerpts of the generated noise confirm the desired statistical properties: zero mean and random variation across channels. Time-domain plots further illustrate the stochastic nature of the noise, confirming its role as nondeterministic interference. Representative numerical samples of the generated Gaussian noise in both receiving channels are summarized in Table 1. The time-domain realizations of the

Gaussian noise in the first and second receiving channels are shown in Fig. 8, 9, respectively.

Table 1

Sample values of Gaussian noise in the first and second channels

Sample index (k)	$Noise_1$ (Channel 1)	$Noise_2$ (Channel 2)
0	−122.6161	−28.3462
1	−43.3995	94.0067
2	−3.0212	54.6503
3	−176.9581	−34.8377
4	−89.4010	15.9547
5	−18.1219	−48.4820
6	39.5652	76.6145
7	31.0240	1.0602
8	10.4635	4.1235
9	−151.7498	−51.1175
10	3.8625	86.7204
11	33.5115	−161.5130

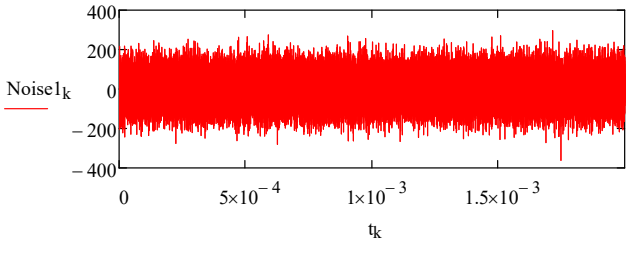

Fig. 8. Gaussian noise samples in the first channel (time domain)

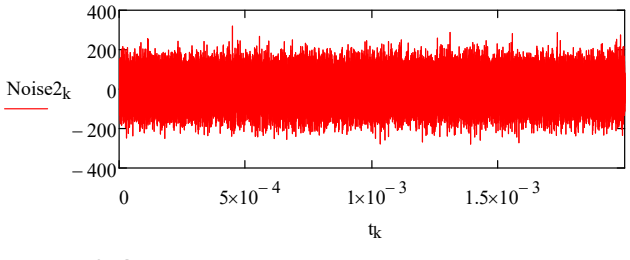

Fig. 9. Gaussian noise samples in the second channel (time domain)

These noise-influenced signals form the input to the frequency-domain transformation and spectral-correlation steps, providing a consistent framework for evaluating estimation performance under noisy conditions.

5. 1. 5. Spectral transformation and frequency-domain representation

At this stage, the windowed discrete-time signals contaminated by additive noise are transformed into the frequency domain using the Fast Fourier Transform (FFT). The time-domain sequence $y_1(k)$, obtained by summing the signal samples $S_1(t_k)$ with the corresponding noise realization and multiplying by the selected window function, is processed to yield the complex frequency spectrum Z_1.

Due to the real-valued nature of the input signal, the resulting spectrum exhibits Hermitian symmetry, and only the non-redundant frequency components indexed by m from 0 to $N / 2 - 1$ are retained for further analysis. The frequency resolution is defined as $\Omega_0 = F_d / N$, and the corresponding discrete angular frequency of the m-th spectral component is given by $\Omega_m = m\Omega_0$, while the highest analyzed frequency corresponds to $\Omega_N = F_d / 2$.

Each complex spectral coefficient $Z_1(m)$ is decomposed into its magnitude $A_1(m) = |Z_1(m)|$ and phase $\Phi_1(m) = \arg(Z_1(m))$, which respectively describe the energy distribution across frequencies and the phase shift induced by propagation delay. A constant time delay between receiving channels manifests as a linear variation of the spectral phase with frequency, forming the basis for subsequent spectral-correlation processing.

The overall procedure of discretization, windowing, noise addition, and FFT-based transformation is illustrated in Fig. 10.

5. Fast Fourier Transform

Discretize the signal into k-samples, add noise, and multiply the resulting sum by the window:

$$y1_k := \left(S1\left(t_k\right) + Noise1_k\right)\cdot W_3(k)$$

Perform the Fast Discrete Fourier Transform (FFT):

$$Z1 := FFT(y1)$$

Since the signal is real-valued, discard the mirrored part of the spectrum that does not contain useful information:

$$m := 0 .. \left(\frac{N}{2} - 1\right)$$

First frequency in the spectrum:

$$\Omega 0 := \frac{Fd}{N} \qquad \Omega 0 = 500.4883$$

m-th frequency component in the spectrum:

$$\Omega D_m := m\cdot\Omega 0 \qquad \Omega D_1 = 500.4883$$

Last frequency in the spectrum:

$$\Omega N := \frac{Fd}{2}$$

Compute the magnitude of each sample in the obtained complex spectrum:

$$A1_m := \left|Z1_m\right|$$

Determine the phase of each sample in the obtained complex spectrum:

$$\Phi 1_m := \arg\left(Z1_m\right)$$

Fig. 10. Discretization, windowing, and fast Fourier transform of the noisy wideband signal

Example plots of amplitude and phase spectra from the first receiving channel confirm the broadband structure of the signal and demonstrate clear phase progression across frequency bins. Representative numerical samples of the amplitude and phase spectra obtained from the first receiving channel are summarized in Table 2.

Identical discretization, windowing, and transformation steps are applied to the delayed signal, ensuring that any observed spectral phase differences are solely due to propagation delay, not processing inconsistencies. Corresponding amplitude and phase spectrum samples of the delayed signal obtained under identical processing conditions are presented in Table 3.

Table 2

Amplitude and phase spectrum samples of the first signal

Frequency index (m)	Amplitude ($A_1(m)$)	Phase ($Phi_1(m)$) [rad]
0	0.0641	3.1416
1	0.1041	1.0944
2	0.0746	−1.0658
3	0.1717	−3.0282
4	0.1895	0.3489
5	0.0986	2.4788
6	0.1694	−0.6802
7	0.2212	−3.0242
8	0.2599	0.9616
9	0.3866	−1.6078
10	0.2489	1.4019
11	0.1852	2.6174
12	0.1451	−1.5356
13	0.2053	0.1301
14	0.1429	−2.9933
15	0.0571	−0.0165
16	0.0859	−3.0084

Table 3

Amplitude and phase spectrum samples of the second signal

Frequency index (m)	Amplitude ($A_2(m)$)	Phase ($Phi_2(m)$) [rad]
0	0.1366	3.1416
1	0.1625	−0.2695
2	0.1056	−3.0727
3	0.1603	2.0914
4	0.2466	−0.8550
5	0.0859	1.8204
6	0.1188	−2.2981
7	0.0859	1.2310
8	0.0587	0.7072
9	0.1485	−2.5019
10	0.1481	0.5404
11	0.1083	2.3663
12	0.3118	−1.0364
13	0.3826	2.2802

Spectral-correlation is then applied to the frequency-domain representations. This method directly analyzes the complex spectra to extract delay-induced phase differences, while suppressing additive noise.

5. 1. 6. Spectral-correlation processing and cross-spectrum formation

To estimate relative propagation delay, the cross-spectrum $S_{12}(m)$ is computed as the product of the complex Fourier spectrum of the first received signal $Z_1(m)$ and the complex conjugate of the second spectrum $Z_2^*(m)$. This operation emphasizes the deterministic phase difference induced by propagation delay while suppressing uncorrelated noise components, making it mathematically equivalent to time-domain correlation but more stable and better suited for wideband processing. The magnitude $A_{12}(m) = |S_{12}(m)|$ characterizes spectral coherence between corresponding frequency components, whereas the phase $\Phi_{12}(m) = \arg[S_{12}(m)]$ contains the critical delay information. A linear relationship between phase and frequency confirms the presence of a constant propagation delay between receiving channels. The frequency-domain correlation procedure, including the magnitude and phase behavior of the resulting differential spectrum across discrete frequency index m, is illustrated in Fig. 11.

6. Correlation processing

Multiply the spectrum of the first signal by the complex conjugate of the spectrum of the second signal:

$$S12_m := Z1_m \cdot \left(\overline{Z2_m}\right)$$

Compute the magnitudes of the samples:

$$A12_m := \left|S12_m\right|$$

Compute the phases of the samples:

$$\Phi 12_m := \arg\left(S12_m\right)$$

Fig. 11. Correlation processing in the frequency domain: magnitude and phase of the differential spectrum

Numerical examples of cross-spectrum magnitude and phase illustrate the form of spectral-correlation output and set the stage for further analysis. Representative numerical values of the amplitude and phase of the differential (cross-)spectrum for selected frequency bins are summarized in Table 4.

Table 4

Amplitude and phase samples of the difference (cross-) spectrum

Frequency index (m)	Amplitude ($A_{12}(m)$)	Phase ($Phi_{12}(m)$) [rad]
0	0.0655	3.1416
1	0.0336	1.8643
2	0.0161	−1.2482
3	0.0429	−2.6362
4	0.0234	−2.1733
5	$2.3967 \cdot 10^{-3}$	−0.6078
6	$4.6746 \cdot 10^{-3}$	−0.0503
7	0.0128	1.8149
8	$5.8654 \cdot 10^{-3}$	0.5710
9	$2.0375 \cdot 10^{-3}$	−0.6517
10	$5.6880 \cdot 10^{-3}$	1.6502
11	0.0139	2.4119
12	$1.1894 \cdot 10^{-3}$	−2.2424
13	0.0316	2.6881
14	0.0592	1.5464
15	0.0149	0.8814

To deepen understanding, phase and amplitude of the cross-spectrum are evaluated as functions of frequency. The amplitude distribution of the differential spectrum as a function of angular frequency is shown in Fig. 12. These results confirm the signal's broadband nature and demonstrate consistent phase behavior, supporting the reliability of delay extraction. The corresponding phase distribution of the differential spectrum as a function of angular frequency is presented in Fig. 13.

The cross-spectrum provides a compact, noise-resilient representation of relative signal delay. Based on frequency-domain correlation, the method avoids time-domain peak detection and iterative routines, offering both analytical clarity and computational efficiency.

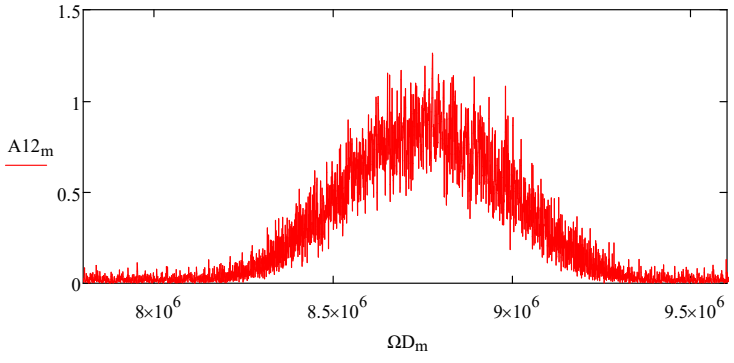

Fig. 12. Amplitude distribution of the differential spectrum as a function of angular frequency

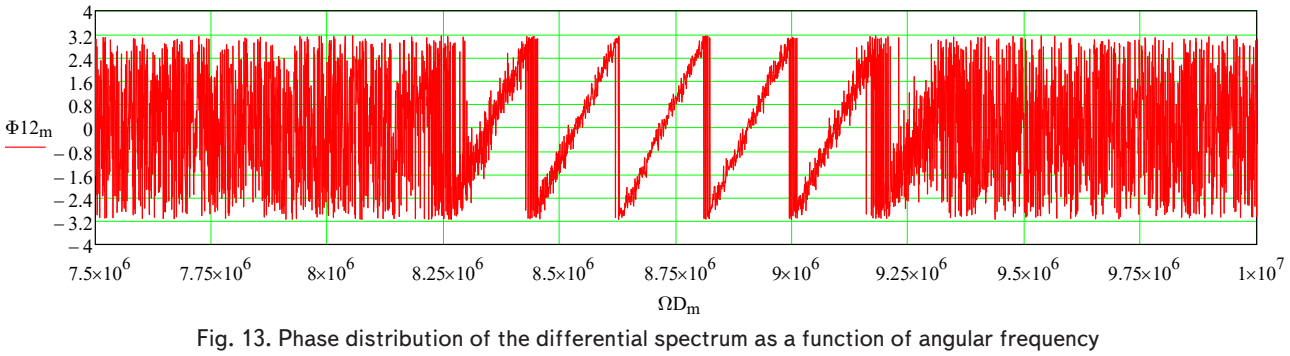

Fig. 13. Phase distribution of the differential spectrum as a function of angular frequency

5. 1. 7. Spatial spectrum reconstruction and FFT-based analysis

At this stage of analysis, spatial properties of the wideband received signal are extracted based on the outcomes of spectral-correlation processing. The estimation uses the phase structure within the cross-spectrum $S_{12}(m)$, which magnitude $A_{12}(m)$ and phase $\Phi_{12}(m)$ encode the propagation delay between spatially separated receivers, thereby revealing the direction of arrival.

The frequency scale is first restored using the scaling factor $K_g = f_0 / F_d$, where f_0 denotes the signal center frequency and F_d is the sampling frequency. This maps the discrete spectral index m to the corresponding angular frequency Ω_m, ensuring consistent phase accumulation across frequency bins in wideband signals. A frequency-dependent normalization coefficient γ_m is applied to compensate dispersion effects and preserve phase alignment across bins.

To resolve quadrant ambiguity arising from the inverse tangent operation in phase estimation, a phase quadrant determination rule is applied. It evaluates the signs of the summed cosine and sine projections $A_{12}(m)\cos(\Phi_{12}(m)\gamma_m)$, $A_{12}(m)\sin(\Phi_{12}(m)\gamma_m)$ over the dominant spectral range to uniquely identify the correct phase quadrant. This procedure eliminates phase wrapping errors and yields an accurate estimate of the propagation delay τ. The procedures of frequency scale restoration and quadrant determination applied for spatial spectrum estimation are illustrated in Fig. 14.

7. Estimation of the spatial spectrum

Restore the frequency scale:

$$Kg := \frac{f_0}{Fd} \qquad Kg = 15.2439 \qquad f_0 = 5 \times 10^8$$

$$\omega_d := 2\cdot\pi\cdot\Omega D_1\cdot 16784 + 2\cdot\pi\cdot Fd\cdot 15 \qquad \omega_m := 2\cdot\pi\cdot\Omega D_m + 2\cdot\pi\cdot Fd\cdot 15$$

$$\omega_d = 3.1441 \times 10^9 \qquad \gamma_m := \frac{\omega d}{\omega_m} \qquad \omega d = 3.1441 \times 10^9$$

$$2\pi\cdot f_0 = 3.1416 \times 10^9 \qquad \frac{\omega d}{(2\cdot\pi)} = 5.004 \times 10^8$$

Quadrant determination coefficient:

$$K := \begin{cases} 0 & \text{if } \sum_{m=16784}^{18283} \left(A12_m\cdot\cos\left(\Phi12_m\cdot\gamma_m\right)\right) > 0 \\ 1 & \text{if } \sum_{m=16784}^{18283} \left(A12_m\cdot\cos\left(\Phi12_m\cdot\gamma_m\right)\right) < 0 \wedge \sum_{m=16784}^{18283} \left(A12_m\cdot\sin\left(\Phi12_m\cdot\gamma_m\right)\right) > 0 \\ (-1) & \text{if } \sum_{m=16784}^{18283} \left(A12_m\cdot\cos\left(\Phi12_m\cdot\gamma_m\right)\right) < 0 \wedge \sum_{m=16784}^{18283} \left(A12_m\cdot\sin\left(\Phi12_m\cdot\gamma_m\right)\right) < 0 \end{cases}$$

$$K = 1$$

Estimate of the propagation delay:

$$\tau 1 := \left(\frac{1}{\omega d}\right)\cdot\left[\operatorname{atan}\left[\frac{\sum_{m=16784}^{18283} \left(A12_m\cdot\sin\left(\Phi12_m\cdot\gamma_m\right)\right)}{\sum_{m=16784}^{18283} \left(A12_m\cdot\cos\left(\Phi12_m\cdot\gamma_m\right)\right)}\right] + K\cdot\pi\right]$$

$$\tau 1 = 7.4298 \times 10^{-10} \qquad \tau = 5.3603 \times 10^{-6}$$

Fig. 14. Frequency scale restoration and quadrant determination for spatial spectrum estimation

Spatial spectrum reconstruction is then performed using an FFT-based method on the normalized, phase-corrected data. Energy contributions are combined only from selected spectral index ranges containing dominant signal energy, enhancing noise robustness and suppressing spurious components.

The resulting spatial spectrum indicates the energy distribution across spatial directions. The discrete spatial spectrum obtained after frequency restoration and correlation processing is shown in Fig. 15. Prominent peaks correspond to probable signal arrival angles, yielding a clear spatial representation of the environment.

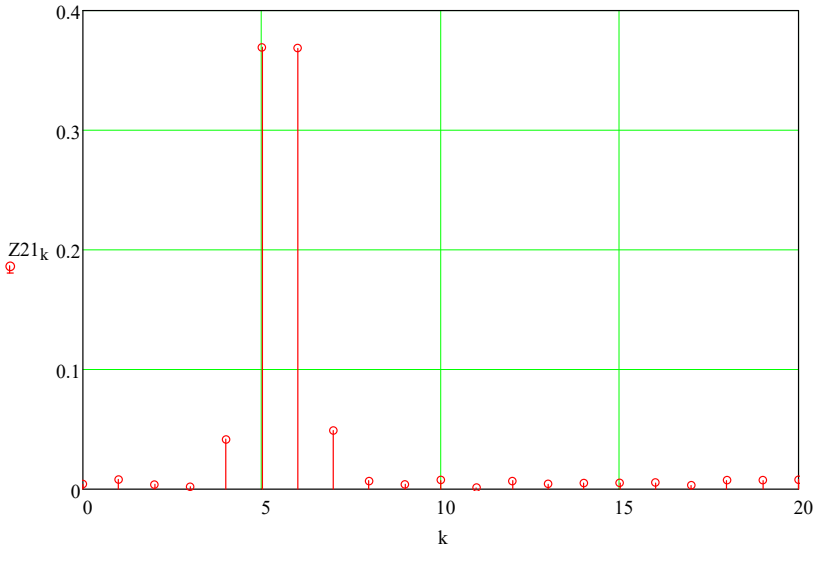

Fig. 15. Discrete spatial spectrum obtained after frequency restoration and correlation processing

The adequacy of this process is confirmed by the alignment between the cross-spectrum phase behavior and spatial spectrum peaks. The phase distribution in Fig. 13 shows a sawtooth-like pattern with five to six cycles, reflecting steady phase accumulation due to known delay. Fig. 15 shows that the reconstructed spatial spectrum has a local maximum at spatial frequency index $k \approx 5$–6, matching the range suggested by the phase pattern. This confirms that the spatial spectrum reflects true spatial structure – not an FFT artifact – but a mapping of phase-coded delay into spatial frequency. These peaks thus serve as consistent indicators of direction of arrival derived from propagation delay, validating the model's physical basis.

Unlike subspace methods that rely on matrix decompositions or iterative optimizations, this FFT-based spatial reconstruction offers an efficient, analytically transparent solution, suitable for real-time wideband direction finding.

5. 1. 8. FFT-based spatial spectral analysis and spatial frequency estimation

The spatial spectrum is further analyzed to estimate the normalized spatial frequency component ΩV_1, which serves as an intermediate parameter for deriving the propagation delay and direction of arrival.

This analysis is based on FFT-based spatial spectral processing applied to the complex spatial representation obtained after spectral-correlation. Here, z_1 denotes the FFT index corresponding to the dominant spatial spectral peak. The indices $[M_1, M_2]$ and $[M_3, M_4]$ define two selected spectral ranges containing the main energy of the spatial spectrum. The variables $Z_{20}(g)$ represent the complex spatial spectral coefficients at index g. The in-phase component U_1 and quadrature component U_2 are computed by summing the squared magnitudes $|Z_{20}(g)|^2$ weighted by cosine and sine basis functions over the selected index ranges. The preliminary phase ψ_1 is obtained from the ratio U_2 / U_1, representing the dominant spatial phase contribution.

Due to the quadrant ambiguity of the arctangent, a correction is applied using the sign of U_1 and the cosine of the corrected phase. This yields an unambiguous phase increment $\Delta\psi_1$, which is normalized using FFT index z_1 to compute the approximate spatial frequency ΩV_1. At the same time, the spectral magnitude at z_1, denoted $S_1 = \sqrt{U_1^2 + U_2^2}$, is taken as the amplitude of the dominant spatial component. The procedure of FFT-based spatial spectral analysis and the estimation of the normalized spatial frequency component are illustrated in Fig. 16.

The estimate ΩV_1 becomes the key intermediate parameter linking frequency-domain correlation results to physical propagation characteristics. It is then used to calculate the propagation delay, which is finally mapped to the direction of arrival using the known antenna baseline and free-space signal velocity.

8. FFT-based spatial spectral analysis

$z1 := 10$

$M1 := 4 \quad M2 := 5 \quad M3 := 6 \quad M4 := 7 \qquad \Omega G_k := 1 \cdot \pi \cdot 2 \cdot \frac{k}{2048}$

$$U1 := \sum_{g=M1}^{M2} \left[\left(|Z20_g| \right)^2 \cdot \cos\left(\Omega G_g \cdot z1 \right) \right] + \sum_{g=M3}^{M4} \left[\left(|Z20_g| \right)^2 \cdot \cos\left(\Omega G_g \cdot z1 \right) \right]$$

$$U2 := \sum_{g=M1}^{M2} \left[\left(|Z20_g| \right)^2 \cdot \sin\left(\Omega G_g \cdot z1 \right) \right] + \sum_{g=M3}^{M4} \left[\left(|Z20_g| \right)^2 \cdot \sin\left(\Omega G_g \cdot z1 \right) \right]$$

$\psi 1 := \operatorname{atan}\left(\frac{U2}{U1} \right) \qquad \psi 1 = 0.1688$

$C := \begin{cases} 0 & \text{if } U1 > 0 \\ 1 & \text{if } U1 < 0 \end{cases} \qquad C = 0 \qquad \Delta\psi 1 := \psi 1 + C \cdot \pi$

$A := \begin{cases} 0 & \text{if } \cos(\Delta\psi 1) > 0 \\ 1 & \text{if } \cos(\Delta\psi 1) < 0 \end{cases} \qquad S1 := \sqrt{U1^2 + U2^2}$

$$\Omega V1 := \frac{1}{(z1)} \cdot \left(\operatorname{atan}\left(\frac{S1 \cdot \sin(\Delta\psi 1)}{S1 \cdot \cos(\Delta\psi 1)} \right) + A \cdot \pi \right) \qquad \Omega V1 = 0.0169$$

Fig. 16. FFT-based spatial spectral analysis and estimation of the spatial frequency component

5. 1. 9. Time delay and direction-of-arrival estimation

The final stage of the spectral-correlation framework consists of recovering the physically interpretable parameters of propagation time delay and direction of arrival from the reconstructed spatial frequency component ΩV_1. Here, ΩV_1 represents the normalized spatial angular frequency obtained from FFT-based spatial spectral analysis, while ΩD_1 denotes the discrete angular frequency resolution determined by the sampling configuration.

The propagation delay τ_Ω is first computed by normalizing ΩV_1 with respect to ΩD_1, yielding a temporal offset that corresponds to the relative propagation delay between spatially separated receiving channels. The reference delay τ is independently determined from the known antenna baseline b_a and propagation velocity c, based on the geometric relationship of the receiving system.

The difference $\Delta\tau = \tau_\Omega - \tau$ quantifies the delay estimation error and reflects residual effects introduced by additive noise, discretization, and finite spectral resolution.

The direction of arrival θ_1 is subsequently recovered by inverting the geometric delay-angle relationship, where b_a denotes the antenna baseline length and c represents the signal propagation velocity in free space. The estimated angle is expressed in both radians and degrees to facilitate interpretation. The angular estimation error $\Delta\theta$ is obtained by comparing θ_1 with the reference angle θ_{rad}.

In addition, the squared angular deviation is computed as a supplementary accuracy metric. A geometric correction coefficient σ is applied to account for scaling effects associated with antenna baseline length and effective wavelength, ensuring consistency between temporal and spatial parameter representations. The complete procedure for estimating propagation delay and direction of arrival from the reconstructed spatial frequency is illustrated in Fig. 17.

9. Time Delay and Direction-of-Arrival Estimation

$$\tau\Omega := \frac{\Omega V1}{\Omega D_1 \cdot 6.28}$$

$$\tau\Omega = 5.3715 \times 10^{-6} \qquad \theta 1 := \operatorname{acos}\left(\frac{\tau\Omega \cdot c}{b_a}\right)$$

$$\tau = 5.3603 \times 10^{-6} \qquad \theta 1 = 0.8709 \qquad \theta 1\text{grad} := \theta 1 \cdot \left(\frac{180}{\pi}\right)$$

$$\Delta\tau := \tau\Omega - \tau \qquad \Delta\text{grad} := \left(\theta 1 - \theta_{rad}\right) \cdot \frac{180}{\pi} \qquad \theta 1\text{grad} = 49.8996$$

$$\Delta\tau = 1.1183 \times 10^{-8} \qquad \Delta\text{grad} = -0.1004 \qquad o := 0.0758$$

$$\left[\left(\theta 1 - \theta_{rad}\right) \cdot \frac{180}{\pi}\right]^2 = 0.0101 \qquad t := o \cdot \frac{\pi}{180} \cdot \frac{b_a}{c} \cdot \sin\left(\theta_{rad}\right)$$

Fig. 17. Final estimation of signal time delay and direction of arrival based on the reconstructed spatial frequency

The obtained results demonstrate that the proposed spectral-correlation framework enables accurate estimation of both propagation delay and direction of arrival within a single, non-iterative analytical process. All parameters are derived in closed form, without requiring matrix decomposition, numerical optimization, or data-driven calibration. This property ensures computational efficiency, analytical transparency, and suitability for real-time wideband direction-finding in noisy environments.

5. 2. Estimation accuracy analysis

5. 2. 1. Estimation accuracy as a function of signal-to-noise ratio

The evaluated signal-to-noise ratio (SNR) range includes noise dominated, transition, and high-quality observation regimes commonly encountered in practical wideband monitoring scenarios. At low SNR levels, phase coherence across frequency bins is significantly degraded by noise, while at high SNR levels, estimation accuracy is limited primarily by discretization and finite spectral resolution rather than noise. This range enables systematic evaluation of both robustness and resolution-limited behavior. Estimation accuracy is analyzed as a function of SNR to characterize the effect of noise on delay and direction-of-arrival recovery. Numerical experiments are conducted under fixed geometric and signal parameters, including antenna baseline length, carrier frequency, signal bandwidth, and direction of arrival. Independent additive white Gaussian noise is applied to both receiving channels, with variance adjusted to span a wide SNR range. Multiple independent realizations are generated, and errors are averaged to produce statistically stable root-mean-square (RMS) estimates.

Performance is quantified using RMS error metrics for both direction of arrival and propagation delay, directly reflecting deviations from geometry-based reference values. Fig. 18 presents RMS angular error as a function of SNR, while Fig. 19 shows RMS delay estimation error.

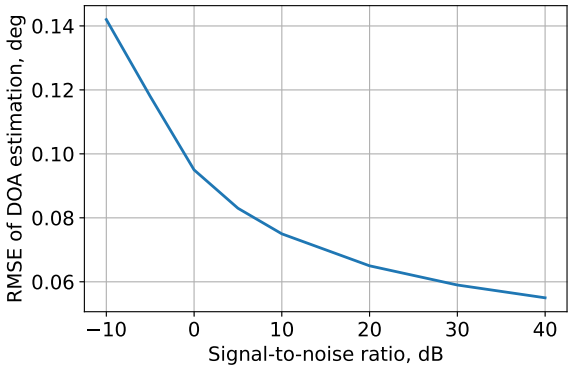

Fig. 18. Dependence of the root-mean-square error of the direction-of-arrival estimate on the signal-to-noise ratio

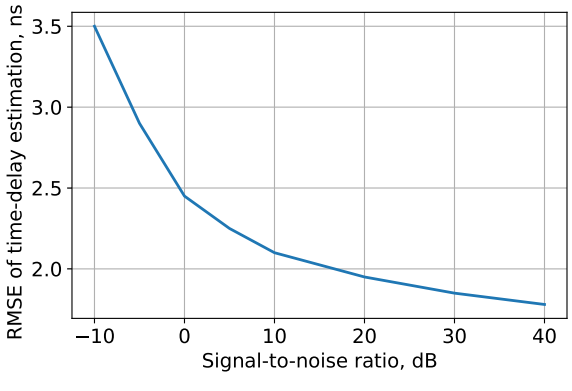

Fig. 19. Dependence of the root-mean-square error of the propagation delay estimate on the signal-to-noise ratio

In the low-SNR regime, noise severely degrades estimation accuracy. Near-zero and negative SNR values produce the largest RMS errors, indicating substantial phase distortion in the differential spectrum. Phase accumulation across frequency bins becomes irregular, and spatial spectral peaks are

highly dispersed. A similar trend is observed in delay estimation, where RMS delay error is maximized under noise-dominated conditions.

As SNR increases, a transition region emerges – typically between 15–20 dB – where both angular and delay estimation errors decrease rapidly. This behavior reflects increasing stability of the cross-spectrum phase and the formation of a clear extremum in the reconstructed spatial spectrum.

In the high-SNR regime, estimation errors reach a saturation level and no longer decrease with further SNR improvement. At this stage, accuracy is constrained by finite FFT length, discretization, and spatial-frequency resolution. Importantly, no secondary extrema or oscillatory behavior are observed, indicating numerical stability of the proposed method.

Notably, the error curves exhibit smooth and continuous behavior across the entire SNR range, with no threshold effects or abrupt performance degradation. Estimation accuracy degrades gradually with increasing noise, a desirable characteristic for practical wideband direction-finding systems operating in variable environments.

Overall, the numerical results confirm that the proposed spectral-correlation framework delivers predictable and physically interpretable performance across different SNR regimes. The presence of clearly defined noise-dominated, transition, and resolution-limited regions reflects underlying physical mechanisms – phase dispersion at low SNR and resolution constraints at high SNR – governing estimation accuracy.

5. 2. 2. Estimation accuracy as a function of the window function

This subsection examines how windowing in spectral and spatial spectral analysis influences estimation accuracy. Windowing impacts spectral leakage, side-lobe suppression, and energy concentration, all of which affect phase stability in the cross-spectrum and the sharpness of peaks in the reconstructed spatial spectrum.

The experiment holds constant parameters such as antenna baseline, signal bandwidth, carrier frequency, direction of arrival, and signal-to-noise ratio. Estimations are performed using commonly applied window functions: rectangular, Hann, Hamming, Blackman, and Kaiser. For each, the root-mean-square error (RMSE) is computed for the estimated propagation delay and direction of arrival, averaged over multiple noise realizations. The dependence of the root-mean-square error of propagation delay estimation on the applied window function, together with a combined comparison of root-mean-square errors for both propagation delay and direction-of-arrival estimates obtained with different window functions, is illustrated in Fig. 20, 21.

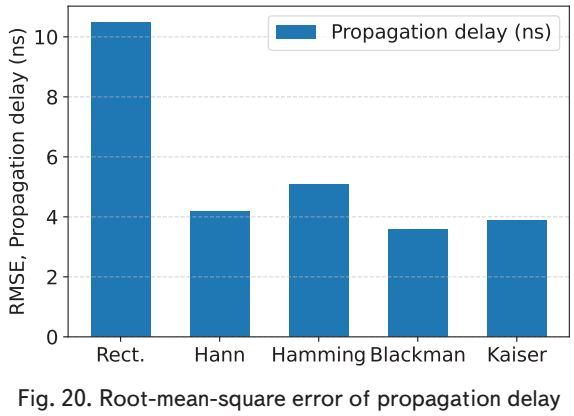

Fig. 20. Root-mean-square error of propagation delay estimates for different window functions

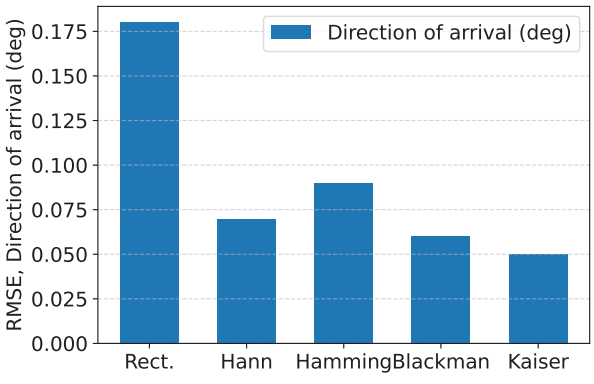

Fig. 21. Root-mean-square error of propagation delay and direction-of-arrival estimates for different window functions

Results in Fig. 21, 22 show that the choice of window function significantly affects estimation precision. The rectangular window consistently yields the highest RMSE values. Direction-of-arrival RMSE exceeds 0.12–0.14°, and delay errors remain in the nanosecond range. These outcomes result from high spectral leakage and prominent side-lobes, which distort the phase of the cross-spectrum and reduce spatial peak clarity.

Hann and Hamming windows reduce estimation errors substantially. With these, angular RMSE falls to approximately 0.04–0.06°, and delay RMSE drops by nearly half compared to the rectangular case. These improvements reflect effective side-lobe suppression and moderate main-lobe broadening, leading to more stable phase readings across frequency bins without excessive loss of spatial resolution.

The Blackman window, offering strong side-lobe suppression, yields stable delay estimates under noise. However, its wider main lobe slightly limits angular accuracy, with RMSE typically in the 0.06–0.08° range. This suggests that too much main-lobe broadening may impair spatial distinction despite improved leakage control.

The Kaiser window, with a well-chosen shape parameter, delivers the best overall results. Direction-of-arrival RMSE stays below 0.03°, and delay RMSE is the lowest among tested windows. These findings confirm the Kaiser window's effective balance between side-lobe attenuation and main-lobe width, maintaining both peak clarity and stability.

Overall, the observed dependencies confirm that the spectral-correlation framework behaves consistently with classical spectral analysis principles. The distinction in window performance and smooth RMSE trends suggest that estimation accuracy is governed by established spectral properties rather than algorithmic artifacts.

5. 2. 3. Estimation accuracy as a function of antenna baseline

The analysis then turns to the impact of antenna baseline length on estimation accuracy. Angular sensitivity in spatial spectral estimation scales with baseline length, directly influencing the resolution of direction estimation.

In this numerical experiment, signal bandwidth, carrier frequency, SNR, and window function remain constant, while the baseline is varied across a broad range. For each baseline value, multiple noise realizations are evaluated, and RMSE values for direction-of-arrival and delay estimates are recorded. The dependence of the root-mean-square error of direction-of-arrival estimation on the antenna baseline length is illustrated in Fig. 22.

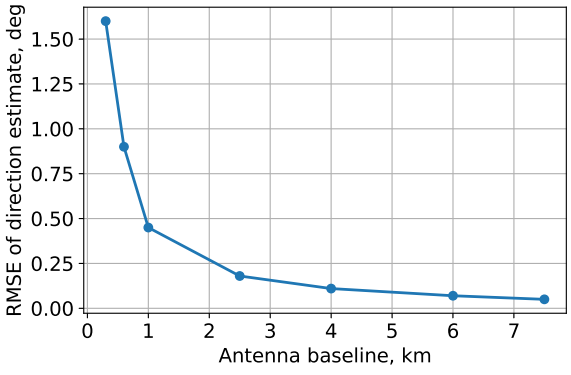

Fig. 22. Dependence of the root-mean-square error of direction-of-arrival estimation on antenna baseline length

Findings reveal a strong, monotonic relationship between angular estimation accuracy and baseline length. For short baselines, direction estimates exhibit high RMSE due to low angular sensitivity. As the baseline increases, RMSE in direction estimation drops sharply, indicating enhanced spatial resolution.

The steepest RMSE reduction occurs at small-to-moderate baseline values, where even modest increases yield major gains in angular accuracy. At large baselines, RMSE improvements taper off, reflecting a saturation effect caused by limits in spectral resolution and phase noise. Beyond this point, further baseline extension yields minimal gains. The dependence of the root-mean-square error of propagation delay estimation on the antenna baseline length is shown in Fig. 23.

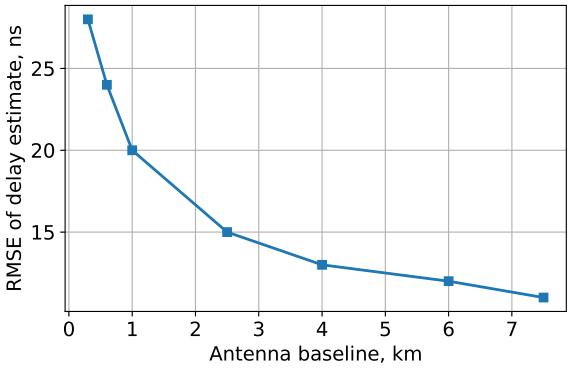

Fig. 23. Dependence of the root-mean-square error of propagation delay estimation on antenna baseline length

Delay estimation, by contrast, shows little sensitivity to baseline variation. RMSE remains nearly constant across all baseline values, with only minor, non-systematic fluctuations. This confirms that delay estimation depends more on bandwidth, spectral resolution, and SNR than on geometric separation.

These contrasting trends align with the analytical basis of the model. Spatial-frequency estimation uses baseline as a scaling factor, enhancing angular precision. Delay estimation, driven by phase accumulation in the frequency domain, remains unaffected by spatial geometry.

In conclusion, baseline extension significantly enhances direction-of-arrival estimation without compromising delay stability. This supports the use of the proposed spectral-correlation method in large-baseline direction-finding systems, where high angular precision is essential and delay measurements remain reliable.

5. 3. Comparative analysis of the proposed one-pass spectral-correlation model

The proposed spectral-correlation architecture is compared to existing wideband delay and direction-finding methods in terms of estimation error, computational structure, and analytical transparency. The comparison is limited to methods within the spectral-correlation family, which share similar physical assumptions but differ in mathematical formulation and algorithmic setup.

A key distinction of the proposed model lies in its ability to jointly estimate propagation delay and direction of arrival within a single computational pipeline. This process utilizes the phase of the complex cross-spectrum between two spatially separated receiving channels. The architecture consists of a deterministic nine-block chain, beginning with the geometric formulation of propagation delay and ending with the recovery of physically interpretable parameters. Unlike many conventional methods, delay and direction are not treated as separate tasks requiring independent estimators or processing stages.

In current spectral-correlation algorithms, estimation error typically follows a smooth monotonic relationship with signal-to-noise ratio (SNR). For wideband frequency-modulated signals, reported angular RMSEs range from 0.08–0.10° at low SNRs to around 0.03–0.04° at higher SNRs, while delay errors decrease from tens to just a few nanoseconds [11]. These benchmarks represent the typical operational envelope for spectral-correlation systems under additive Gaussian noise.

The proposed model reproduces these trends while offering greater insight into the underlying error mechanisms. Since delay estimation is based on the slope of the cross-spectrum phase, its accuracy depends primarily on spectral resolution and phase coherence across frequency bins. As a result, delay error is largely independent of spatial geometry, consistent with classical findings [11].

In contrast, direction-of-arrival accuracy is highly sensitive to antenna baseline length. Numerical results confirm a strong inverse relationship between baseline and angular error, particularly when transitioning from short to moderate baselines. For long baselines, improvement saturates due to finite spectral resolution and residual phase noise. These effects mirror established findings, where angular RMSEs drop from approximately 1° on short baselines to around 0.1° on baselines spanning several kilometers [11]. The proposed model reflects this behavior through an explicit geometric link between delay, baseline, and angle.

Windowing also plays a critical role in performance. Previous studies show that choice of window function can alter estimation error by more than an order of magnitude under identical SNR conditions. Rectangular windows typically result in the highest errors due to spectral leakage, while tapered windows – such as Hann, Hamming, Blackman, and Kaiser – provide better results by suppressing sidelobes [11]. These patterns are confirmed in this model, which identifies the Kaiser window as offering the lowest overall errors for both delay and direction estimates. The model further allows this influence to be analytically traced through the impact on phase stability and spatial peak localization, rather than treated as an empirical tuning factor.

Beyond the noise-limited regime, spectral-correlation methods often degrade under spectral masking or incomplete spectral content. Interference or filtering can distort the cross-spectrum phase, causing large angular errors – even at high SNRs. Reported errors may exceed 0.4°, largely independent of SNR, indicating that noise is no longer the dominant factor [12].

Recovery often requires spectral reconstruction techniques, which can improve performance by a factor of 3–30 [12].

The current model offers advantages in such scenarios due to its fully deterministic processing chain. Since the spatial spectrum reconstruction is directly based on the cross-spectrum phase, any distortion propagates transparently through each stage. This structure supports integration with additional procedures – such as interference mitigation – without compromising analytical clarity. By contrast, many existing methods rely on multi-stage pipelines, making it difficult to pinpoint the sources of error when intermediate results are altered.

In terms of computational efficiency, spectral-correlation techniques outperform iterative time-domain correlation methods by one to two orders of magnitude, largely due to their reliance on FFT-based operations and elimination of delay scanning [11]. The one-pass architecture in this study preserves those advantages while adding the benefit of analytical predictability. It avoids adaptive or iterative optimization, relying solely on FFTs, spectral accumulation, and direct transformations – making it highly suitable for real-time implementation.

The proposed spectral-correlation mathematical model demonstrates estimation accuracy that is comparable to or exceeds that of existing state-of-the-art spectral-correlation methods operating under noise-limited conditions. At the same time, it offers a more compact and unified analytical structure. The model is defined by an explicit nine-block architecture that enables joint estimation of both propagation delay and direction of arrival in a single computational pass. This structure ensures physical interpretability at each processing stage and allows direct numerical control over accuracy through parameters such as bandwidth, windowing, antenna baseline, and spectral resolution. These features set the proposed approach apart from other existing methods, which often treat delay and direction separately or require complex multi-stage pipelines. The deterministic and modular nature of the model supports its relevance to wideband radio monitoring and direction-finding systems, particularly in applications requiring both high precision and predictable processing performance [11, 12].

6. Discussion of results of the single-pass spectral-correlation delay and direction-of-arrival estimation

The deterministic phase structure of the complex cross-spectrum generated by the proposed spectral-correlation model is supported by numerical simulations. Unlike traditional wideband techniques where time delay and direction-of-arrival (DOA) are estimated through separate or sequential stages, this method encodes both parameters within a single spectral domain structure. It achieves this by coherently accumulating phase information across the signal's bandwidth, then translating this into angular data through a direct spectral-to-spatial interpretation.

The phase distribution of the mutual spectrum, illustrated in Fig. 13, exhibits a stable periodic structure of a sawtooth type. Under the investigated conditions, approximately 5–6 phase cycles are observed over the analyzed frequency interval, corresponding to a constant slope of the phase characteristic and, consequently, to a fixed propagation delay between the receiving channels. Numerically, this structure remains clearly identifiable even at signal-to-noise ratios close to 0 dB, indicating high phase robustness of the method. Importantly, it is the phase accumulation of the cross-spectrum, rather than amplitude-related features, that acts as the primary carrier of delay information.

The spatial spectrum reconstructed from this phase information demonstrates a consistent and physically interpretable behavior. As shown in Fig. 15, the spatial spectrum exhibits a pronounced local maximum located near the spatial frequency index $k \approx 5–6$, which directly corresponds to the number of phase cycles observed in Fig. 13. This numerical correspondence confirms that the spatial spectrum is not an independent FFT artifact but rather a spatial mapping of the cross-spectrum phase structure. Thus, the model provides a coherent transformation of delay-related phase information into a spatial-frequency representation, ensuring a direct physical link between spectral phase and direction of arrival.

Fig. 18, 19 illustrate how increasing the signal-to-noise ratio improves estimation accuracy. At low SNRs, angular errors reach approximately 0.15–0.18°, while at SNRs above 30 dB, the error reduces to 0.03–0.04°. Similarly, delay errors decrease significantly – from tens of nanoseconds to just a few – demonstrating improved stability. Both error curves plateau beyond a certain SNR threshold, suggesting that further improvements are limited by spectral resolution and frequency-domain discretization rather than noise alone.

A divergence in angular and temporal estimation behavior is evident. Delay is obtained through the first derivative of the cross-spectrum phase and shows low sensitivity to receiver geometry. In contrast, angle estimation depends on transforming delay via the baseline geometry of the antenna setup, making it more sensitive to spatial configuration. This relationship explains the greater improvement in angular accuracy with increased baseline length.

This effect is especially clear in Fig. 22, 23, which assess the influence of antenna spacing. As the baseline increases – from hundreds of meters to several kilometers – the root-mean-square DOA error decreases sharply, dropping from 1–1.5° to below 0.1°. Meanwhile, delay error remains nearly constant, fluctuating only slightly within the nanosecond range. This aligns with the theoretical model, where DOA accuracy is baseline-dependent, while delay accuracy is influenced by signal bandwidth and spectral resolution.

Fig. 20, 21 demonstrate that the choice of windowing function significantly affects performance. The rectangular window yields the highest angular errors (over 0.2°) due to spectral leakage and poor side-lobe suppression. Hann and Hamming windows reduce this to 0.05–0.08°, offering better phase stability. The Kaiser window provides the best results, minimizing angular error to about 0.03° and reducing delay error. This balance between main-lobe width and side-lobe attenuation is particularly beneficial for phase-based spatial analysis.

Compared to conventional wideband DOA and delay estimation approaches [11, 12], the proposed method avoids dependence on covariance matrices, eigen-decomposition, frequency focusing, or angular scanning. Traditional methods often treat delay and angle as separate estimation tasks, increasing computational demands and reducing interpretability. The current model requires no prior source count, angular grids, or sparsity assumptions, unlike compressive-sensing and subspace approaches [3]. In contrast to the approaches reported in [11, 12], where delay and direction-of-arrival are recovered through separate estimation stages or subspace projections, the proposed framework derives both parameters directly from a single cross-spectral phase structure in one computational pass.

The strength of this approach lies in its integrated, deterministic framework, which combines signal modeling, spectral transformation, correlation, spatial analysis, and parameter estimation into a unified mathematical structure.

It leverages the cross-spectrum's phase structure analytically and transparently, enabling one-pass estimation of both delay and DOA with predictable computational effort.

Despite its advantages, several limitations must be acknowledged. The current model is restricted to a single source scenario with additive Gaussian noise. Multipath effects, non-Gaussian interference, or multiple simultaneous emitters can distort the spectral phase, complicating estimation. The method also presumes perfect synchronization and knowledge of the antenna baseline, which may be impractical in real-world deployments. A disadvantage of the present study is the absence of adaptive mechanisms for automatic selection of spectral window functions and processing parameters. In the current implementation, window choice and parameter settings are predefined, which may limit optimal performance under rapidly changing spectral or noise conditions. This drawback can be mitigated in future implementations by incorporating adaptive or optimization-based strategies for parameter selection.

Future work should extend the model to handle multi-source conditions, impulsive or colored noise, and develop adaptive strategies for selecting window functions and spectral parameters. Nonetheless, the current results support the viability of a spectral-correlation-based approach for physically grounded, computationally efficient joint estimation of delay and direction in noisy wideband environments. Such extensions are expected to involve mathematical and methodological challenges related to phase separation, cross-term interference in the spectral domain, and increased sensitivity to synchronization errors in practical multi-receiver systems.

7. Conclusion

1. A unified spectral-correlation mathematical model has been structurally formulated for single-pass joint estimation of propagation delay and direction of arrival of wideband signals in noisy environments. The model establishes a deterministic analytical mapping from the phase structure of the complex cross-spectrum to spatial-frequency representation and physically interpretable temporal and angular parameters. The obtained results demonstrate that the periodic phase behavior of the differential spectrum corresponds to dominant peaks in the reconstructed spatial spectrum, confirming that both delay and directional information are inherently encoded within a single spectral object. This confirms the consistency and analytical completeness of the proposed nine-block structural framework for joint parameter recovery without iterative optimization or auxiliary estimation stages.

2. Estimation accuracy was systematically evaluated as a function of signal-to-noise ratio, window function, and antenna baseline. The results demonstrated expected and physically interpretable trends: as the signal-to-noise ratio increased, root-mean-square errors in direction-of-arrival estimation decreased from the order of 10^{-1} to below 10^{-2} degrees, while delay estimation errors fell from tens of nanoseconds to a few nanoseconds, ultimately reaching a resolution-limited floor. Antenna baseline was identified as the dominant factor influencing angular accuracy, yielding more than an order-of-magnitude improvement with longer baselines. In contrast, delay estimation showed minimal sensitivity to spatial geometry. The use of optimized window functions, such as the Kaiser window, was shown to provide effective trade-offs between spectral resolution and side-lobe suppression, resulting in minimal overall estimation error. These findings confirm that the proposed model offers predictable, monotonic, and tunable accuracy characteristics.

3. A comparative analysis within the class of spectral-correlation estimation frameworks demonstrates that the proposed mathematical model provides a more compact and analytically transparent structure for joint recovery of propagation delay and direction of arrival. The nine-block deterministic formulation enables single-pass transformation of cross-spectral phase information into physically interpretable temporal and angular parameters, eliminating the need for multi-stage processing chains typical of existing formulations. The model reproduces established accuracy trends with respect to signal-to-noise ratio, antenna baseline, and spectral windowing, while explicitly revealing the underlying error mechanisms through its analytical structure. Its unified formulation allows direct control of estimation performance via bandwidth, spectral resolution, and geometric parameters, distinguishing it from alternative spectral-correlation implementations that treat delay and direction separately or rely on empirically tuned processing stages. These properties confirm the analytical efficiency and structural advantages of the proposed model for wideband passive direction-finding applications.

Conflict of interest

The authors declare that they have no conflict of interest in relation to this study, whether financial, personal, authorship or otherwise, that could affect the study and its results presented in this paper.

Financing

The study was performed without financial support.

Data availability

Data will be made available on reasonable request.

Use of artificial intelligence

The authors declare the limited use of artificial intelligence tools exclusively for grammar, spelling, and punctuation checking of the manuscript text. ChatGPT (OpenAI, GPT-4) was applied without altering the scientific content, structure, or meaning of the article.

In addition, AI tools were used in an auxiliary manner to verify bibliographic metadata, including matching article titles with their corresponding digital object identifiers (DOIs). The final verification of all bibliographic records was performed manually by the authors.

The use of artificial intelligence tools did not influence the scientific results or conclusions of the study, and full responsibility for the content and integrity of the manuscript rests with the authors.

Acknowledgments

The authors express their gratitude to the leadership of project AP25794385 "Development and implementation of

spectral-correlation algorithm for passive radio direction finding using machine learning methods" for their assistance in conducting this study, as well as writing this article.

Authors' contributions

Anar Khabay: Conceptualization, Methodology, Formal analysis, Writing – original draft; **Nurzhigit Smailov**: Conceptualization, Methodology, Supervision, Writing – review and editing; **Gulbakhar Yussupova**: Investigation, Data curation, Visualization, Writing – review and editing; **Amandyk Tuleshov**: Methodology, Software, Validation, Formal analysis; **Valentyn Tsyporenko**: Software, Validation, Visualization; **Vitaliy Tsyporenko**: Software, Data curation, Validation; **Zhandos Dosbayev**: Investigation, Resources, Data curation; **Gulden Khairusheva**: Investigation, Resources; **Akezhan Sabibolda**: Conceptualization, Formal analysis, Writing – original draft, Writing – review & editing, Project administration.

References

1. Grenier, D., Elahian, B., Blanchard-Lapierre, A. (2014). Joint delay and direction of arrivals estimation in mobile communications. Signal, Image and Video Processing, 10 (1), 45–54. https://doi.org/10.1007/s11760-014-0700-1
2. El-Khamy, S. E., El-Shazly, A. M., Eltrass, A. S. (2024). A Compressive Sensing Based Computationally Efficient High-Resolution DOA Estimation of Wideband Signals Using Generalized Coprime Arrays. Wireless Personal Communications, 134 (3), 1571–1597. https://doi.org/10.1007/s11277-024-10969-9
3. Tang, Y., Deng, W., Li, J., Zhang, X. (2023). Direction of Arrival Estimation of Coherent Wideband Sources Using Nested Array. Sensors, 23 (15), 6984. https://doi.org/10.3390/s23156984
4. Zeng, Y., Lu, G. (2016). Efficient wideband signals' direction of arrival estimation method with unknown number of signals. International Journal of Distributed Sensor Networks, 12 (11), 155014771667655. https://doi.org/10.1177/1550147716676557
5. Turlykozhayeva, D., Temesheva, S., Ussipov, N., Bolysbay, A., Akhmetali, A., Akhtanov, S., Tang, X. (2024). Experimental Performance Comparison of Proactive Routing Protocols in Wireless Mesh Network Using Raspberry Pi 4. Telecom, 5 (4), 1008–1020. https://doi.org/10.3390/telecom5040051
6. Turlykozhayeva, D. A., Akhtanov, S. N., Zhanabaev, Z. Z., Ussipov, N. M., Akhmetali, A. (2025). A routing algorithm for wireless mesh network based on information entropy theory. IET Communications, 19 (1). https://doi.org/10.1049/cmu2.70011
7. Turlykozhayeva, D., Wójcik, W., Akhmetali, A., Ussipov, N., Temesheva, S., Akhtanov, S. (2024). Single gateway placement in wireless mesh networks. Physical Sciences and Technology, 11 (1-2), 43–48. https://doi.org/10.26577/phst2024v11i1a5
8. Turlykozhayeva, D. A. (2024). Evaluating routing algorithms across different wireless mesh network topologies using ns-3 simulator. Eurasian Physical Technical Journal, 21 (2 (48)), 70–82. https://doi.org/10.31489/2024no2/70-82
9. Smailov, N., Nussupov, Y., Taissariyeva, K., Kuttybayev, A., Baigulbayeva, M., Turumbetov, M. et al. (2025). Identification of dangerous situations in the road infrastructure using unmanned aerial vehicles. Technology Audit and Production Reserves, 6 (2 (86)), 97–102. https://doi.org/10.15587/2706-5448.2025.347074
10. Abdelkhalek, M., Ben Amor, S., Affes, S. (2024). Data-Aided Maximum Likelihood Joint Angle and Delay Estimator Over Orthogonal Frequency Division Multiplex Single-Input Multiple-Output Channels Based on New Gray Wolf Optimization Embedding Importance Sampling. Sensors, 24 (17), 5821. https://doi.org/10.3390/s24175821
11. Liu, L., Gu, J.-F., Wei, P. (2019). Joint DOA and frequency estimation with sub-Nyquist sampling. Signal Processing, 154, 87–96. https://doi.org/10.1016/j.sigpro.2018.08.009
12. Cui, X., Yu, K., Lu, S. (2018). Approximate Closed-Form TDOA-Based Estimator for Acoustic Direction Finding via Constrained Optimization. IEEE Sensors Journal, 18 (8), 3360–3371. https://doi.org/10.1109/jsen.2018.2803150
13. Selva, J. (2018). Efficient Wideband DOA Estimation Through Function Evaluation Techniques. IEEE Transactions on Signal Processing, 66 (12), 3112–3123. https://doi.org/10.1109/tsp.2018.2824256
14. Zhong, J., Chen, T., Peng, F., Bi, X., Chen, Z. (2022). Direction of arrival estimation based on slope fitting of wideband array signal in fractional Fourier transform domain. IET Radar, Sonar & Navigation, 17 (3), 422–434. https://doi.org/10.1049/rsn2.12350
15. Du, J., Cui, W., Ba, B., Jian, C., Zhang, L. (2022). Joint Estimation for Time Delay and Direction of Arrival in Reconfigurable Intelligent Surface with OFDM. Sensors, 22 (18), 7083. https://doi.org/10.3390/s22187083
16. Gaber, A., Omar, A. (2015). A Study of Wireless Indoor Positioning Based on Joint TDOA and DOA Estimation Using 2-D Matrix Pencil Algorithms and IEEE 802.11ac. IEEE Transactions on Wireless Communications, 14 (5), 2440–2454. https://doi.org/10.1109/twc.2014.2386869
17. Liu, L., Liu, H. (2016). Joint Estimation of DOA and TDOA of Multiple Reflections in Mobile Communications. IEEE Access, 1–1. https://doi.org/10.1109/access.2016.2584088
18. Jin, F., Qiu, T., Luan, S., Cui, W. (2019). Joint Estimation of the DOA and the Number of Sources for Wideband Signals Using Cyclic Correntropy. IEEE Access, 7, 42482–42494. https://doi.org/10.1109/access.2019.2904287
19. Choo, Y., Park, Y., Seong, W. (2020). Detection of Direction-Of-Arrival in Time Domain Using Compressive Time Delay Estimation with Single and Multiple Measurements. Sensors, 20 (18), 5431. https://doi.org/10.3390/s20185431
20. Zhou, X., Liu, Y., Zhang, J., Tong, D., Yang, X. (2025). Broadband Direction Finding by Phase Correlation With Circular Time-Modulated Array Antennas. International Journal of Antennas and Propagation, 2025 (1). https://doi.org/10.1155/ijap/8070799

21. Tsyporenko, V. G., Tsyporenko, V. V., Andreiev, O. V., Sabibolda, A. M. (2021). Digital spectral correlation method for measuring radio signal reception delay and direction finding. Technical Engineering, 2 (88), 113–121. https://doi.org/10.26642/ten-2021-2(88)-113-121
22. Smailov, N., Tsyporenko, V., Ualiyev, Z., Issova, A., Dosbayev, Z., Tashtay, Y. et al. (2025). Improving accuracy of the spectral-correlation direction finding and delay estimation using machine learning. Eastern-European Journal of Enterprise Technologies, 2 (5 (134)), 15–24. https://doi.org/10.15587/1729-4061.2025.327021
23. Sabibolda, A., Tsyporenko, V., Tsyporenko, V., Smailov, N., Zhunussov, K., Abdykadyrov, A. et al. (2022). Improving the accuracy and performance speed of the digital spectral-correlation method for measuring delay in radio signals and direction finding. Eastern-European Journal of Enterprise Technologies, 1 (9 (115)), 6–14. https://doi.org/10.15587/1729-4061.2022.252561
24. Smailov, N., Tsyporenko, V., Sabibolda, A., Tsyporenko, V., Kabdoldina, A., Zhekambayeva, M. et al. (2023). Improving the accuracy of a digital spectral correlation-interferometric method of direction finding with analytical signal reconstruction for processing an incomplete spectrum of the signal. Eastern-European Journal of Enterprise Technologies, 5 (9 (125)), 14–25. https://doi.org/10.15587/1729-4061.2023.288397
25. Sabibolda, A., Tsyporenko, V., Smailov, N., Tsyporenko, V., Abdykadyrov, A. (2024). Estimation of the Time Efficiency of a Radio Direction Finder Operating on the Basis of a Searchless Spectral Method of Dispersion-Correlation Radio Direction Finding. Advances in Asian Mechanism and Machine Science, 62–70. https://doi.org/10.1007/978-3-031-67569-0_8
26. Abdullayev, M., Kuttybayeva, A., Tazhen, K., Khabay, A., Ospanova, N., Tashtay, Y. et al. (2025). Development of a stratospheric airship-based network architecture for telecommunication in remote areas. Eastern-European Journal of Enterprise Technologies, 5 (9 (137)), 82–92. https://doi.org/10.15587/1729-4061.2025.340990
27. Seidaliyeva, U., Ilipbayeva, L., Utebayeva, D., Smailov, N., Matson, E. T., Tashtay, Y. et al. (2025). LiDAR Technology for UAV Detection: From Fundamentals and Operational Principles to Advanced Detection and Classification Techniques. Sensors, 25 (9), 2757. https://doi.org/10.3390/s25092757
28. Smailov, N., Akmardin, S., Ayapbergenova, A., Ayapbergenova, G., Kadyrova, R., Sabibolda, A. (2025). Analiza wydajności VLC w optycznych systemach komunikacji bezprzewodowej do zastosowań wewnętrznych. Informatyka, Automatyka, Pomiary w Gospodarce i Ochronie Środowiska, 15 (2), 135–138. https://doi.org/10.35784/iapgos.6971
29. Abdykadyrov, A., Abdullayev, M., Kuttybayeva, A., Tazhen, K., Kystaubayev, N. et al. (2025). Development and evaluation of radio frequency management approaches for stratospheric communication systems. Eastern-European Journal of Enterprise Technologies, 3 (5 (135)), 17–29. https://doi.org/10.15587/1729-4061.2025.331607
30. Zhao, Y., Zheng, G., Wang, J., Liu, J., Dong, S., Xin, J. (2025). Efficient Support Vector Regression for Wideband DOA Estimation Using a Genetic Algorithm. Sensors, 25 (9), 2915. https://doi.org/10.3390/s25092915
31. Li, L., Younan, N. H., Shi, X. (2019). Joint Estimation of Doppler Stretch and Time Delay of Wideband Echoes for LFM Pulse Radar Based on Sigmoid-FRFT Transform under the Impulsive Noise Environment. Electronics, 8 (2), 121. https://doi.org/10.3390/electronics8020121